

PAPER • OPEN ACCESS

Self-adjusting voxelated electrochemical three-dimensional printing of metallic microstructures

To cite this article: Xianghe Meng *et al* 2025 *Int. J. Extrem. Manuf.* **7** 015102

View the [article online](#) for updates and enhancements.

You may also like

- [Crystallinity characterization of white matter in the human brain](#)
Erin G Teich, Matthew Cieslak, Barry Giesbrecht et al.
- [Efficient radiation treatment planning based on voxel importance](#)
Sebastian Mair, Anqi Fu and Jens Sjölund
- [Numerical investigation reveals challenges in measuring the contrast recovery coefficients in PET](#)
Reimund Bayerlein, Benjamin A Spencer, Yasser G Abdelhafez et al.

Self-adjusting voxelated electrochemical three-dimensional printing of metallic microstructures

Xianghe Meng¹ , Xiaomo Wu¹, Xingjian Shen, Yan Xu, Hao Zhang* ,
Mingjun Chen  and Hui Xie* 

State Key Laboratory of Robotics and Systems, Harbin Institute of Technology, Harbin 150080, People's Republic of China

E-mail: haoz@hit.edu.cn and xiehui@hit.edu.cn

Received 21 February 2024, revised 19 April 2024

Accepted for publication 14 October 2024

Published 5 November 2024



Abstract

Microscale metallic structures enhanced by additive manufacturing technology have attracted extensive attention especially in microelectronics and electromechanical devices. Meniscus-confined electrodeposition (MCED) advances microscale 3D metal printing, enabling simpler fabrication of superior metallic microstructures in air without complex equipment or post-processing. However, accurately predicting growth rates with current MCED techniques remain challenging, which is essential for precise structure fabrication and preventing nozzle clogging. In this work, we present a novel approach to electrochemical 3D printing that utilizes a self-adjusting, voxelated method for fabricating metallic microstructures. Diverging from conventional voxelated printing which focuses on monitoring voxel thickness for structure control, this technique adopts a holistic strategy. It ensures each voxel's position is in alignment with the final structure by synchronizing the micropipette's trajectory during deposition with the intended design, thus facilitating self-regulation of voxel position and reducing errors associated with environmental fluctuations in deposition parameters. The method's ability to print micropillars with various tilt angles, high density, and helical arrays demonstrates its refined control over the deposition process. Transmission electron microscopy analysis reveals that the deposited structures, which are fabricated through layer-by-layer (voxel) printing, contain nanotwins that are widely known to enhance the material's mechanical and electrical properties. Correspondingly, *in situ* scanning electron microscopy (SEM) microcompression tests confirm this enhancement, showing these structures exhibit a compressive yield strength exceeding 1 GPa. The indentation tests provided an average hardness of 3.71 GPa, which is the highest value reported in previous work using MCED. The resistivity measured by the four-point probe method was $(1.95 \pm 0.01) \times 10^{-7} \Omega\cdot\text{m}$, nearly 11 times that of bulk copper. These findings demonstrate the considerable advantage of this technique in fabricating complex metallic microstructures with enhanced mechanical properties, making it suitable for advanced applications in microsensors, microelectronics, and micro-electromechanical systems.

¹ These authors contributed equally to this work.

* Authors to whom any correspondence should be addressed.



Original content from this work may be used under the terms of the [Creative Commons Attribution 4.0 licence](https://creativecommons.org/licenses/by/4.0/). Any further distribution of this work must maintain attribution to the author(s) and the title of the work, journal citation and DOI.

Supplementary material for this article is available [online](#)

Keywords: additive manufacturing, self-adjusting voxelated electrodeposition, metallic microstructures 3D printing, nanotwinned copper

1. Introduction

Additive manufacturing (AM) has always been a focus of interest and significantly changes the way we design and process structures at the microscale. A standout technique in this domain is nonlinear laser lithography, which leverages nonlinear light absorption for nanoscale precision in photochemical processes [1, 2]. This approach has enabled the creation of complex and intricate structures, ranging from microscale multi-lens [3] to chiral mechanical metamaterials [4] and soft microrobots with picoforce springs [5]. However, the AM of polymers, primarily relying on photocurable materials, faces limitations in electrical and mechanical properties. These constraints have spurred a shift towards the AM of metals, seeking to leverage their high conductivity, density, and strength for more demanding applications such as microsensors [6, 7], microelectronics [8], and microelectromechanical systems [9, 10].

For metals, many 3D microscale manufacturing methods have been proposed. Among these, electron beam melting (EBM) and selective laser melting are the most established, allowing for selectively melting metal particles with a focused electron or laser beam, which then form into a solid structure [11]. Focused ion beams (FIB) are also extensively used in manufacturing applications, and similar in principle, focused electron beam induced deposition and FIB induced deposition (FIBID) have achieved further reduction in the scale of manufacture to less than 10 nm [12, 13]. However, the need for special conditions like vacuum and precursor gas in these methods, coupled with the difficulty in obtaining ideal precursors, often leads to contamination and diminished mechanical and electrical properties in the produced metal structures [14].

Furthermore, recent advancements such as direct ink writing [15–17], electrohydrodynamic printing [18, 19], and laser-induced forward transfer [20, 21] have emerged. These techniques typically use pressure or laser jetting of metal nanoparticle inks to form structures with a looser internal configuration, often requiring high-temperature annealing to enhance their mechanical and electrical properties. Additionally, while the adaptation of these techniques for metals, through two-photon induced metal ion reduction [22, 23] and surface functionalization [24], including physical or chemical copper plating [25], is complex. The aggregation of metal particles and non-uniform particle distribution contribute to surfaces that are not smooth and structures that are not dense, resulting in poor mechanical properties.

Another approach, which enables high-throughput and high-resolution fabrication of magnetic polymers or metals, is

achieved by combining stereolithography with template electrodeposition, where the template is fabricated by direct laser writing [26, 27]. However, this method involves complex pre-processing and post-processing steps, and maskless fabrication has not yet been achieved.

Electrochemical AM provides an advantageous alternative to conventional methods, enabling the production of pure metals without the need for complex post-processing. The meniscus-confined electrodeposition (MCED) technique simplifies experimental setups by employing a metal wire as the anode within a micropipette filled with electrolyte, positioned in contact with a cathodic metal substrate. This technique is particularly effective for interconnecting 3D microdevice components [28]. Furthermore, this continuous MCED method has successfully produced metal wires as thin as ~ 150 nm in an air environment [29].

Building on this technology, another advancement involved the creation of hollow structures using pulsed voltages with variable duty cycles. It was found that the evaporation-induced convective flow during nonpotential periods leads to preferential deposition at the edges of structures [30]. Moreover, in the continuous MCED process of fabricating copper structures, the application of pulsed voltage has been shown to result in the formation of nanotwinned (nt) metals [31, 32], thereby enhancing both the mechanical and electrical properties of these metals [33].

Although continuous electrochemical deposition can produce a variety of shapes, it faces challenges in creating densely packed structures and requires precise control over the nozzle withdrawal rate to prevent clogging. The integration of an atomic force microscopy (AFM) closed-loop control system can help mitigate the clogging issue [34]. However, it introduces additional complexity to the equipment and control mechanisms.

A different method, layer-by-layer (voxel) printing, utilizes a FluidFM tip, which is an AFM tip featuring an integrated fluid microchannel. This technique identifies contact with the structure being fabricated by the bending of the AFM cantilever, leading to laser beam deflection and the formation of thin layers [35]. This process enables the creation of intricate structures and dense metal arrays [36, 37]. However, it necessitates operation within a liquid electrolyte environment to function effectively.

A subsequent advancement involved a method for voxel printing in air, enabling the fabrication of high-density and high aspect ratio metal micro- and nano-arrays using current feedback. This process involves monitoring the deposition current to dynamically control the contact and detachment of the micropipette from the substrate. Once a single layer is

completed, the nozzle moves to the next position for continued printing. Moreover, the intermittent nature of layer-by-layer printing enhances evaporation, leading to faster deposition rates than continuous deposition [38]. This approach also achieved a significant reduction in the minimum deposition size possible with the MCED method, down to 25 nm [39]. While voxel printing permits the creation of complex and array structures with MCED, the decreasing scale of deposition makes it increasingly challenging to accurately estimate the thickness of individual voxel, complicating the determination of the exact shape and size of the final deposition. Thus, there is a clear need for development of a novel MCED strategy based on voxelated electrochemical 3D printing to address the issue where the final structure's shape depends on the estimated voxel thickness, which is inevitably subject to errors due to experimental disturbances.

In this work, we present a novel electrochemical voxelated AM approach for fabricating three-dimensional metallic structures, which eliminates the need to estimate voxel thickness for the control of the printing process. The dimensions of the deposited features are primarily determined by the trajectory of the micropipette, which is precisely controlled and aligned with the predetermined printing structures through a high-precision motion system. As a consequence of this alignment, the voxel position automatically adjusts in response to the micropipette's movement, offering compensation for uncontrollable environmental fluctuations. We demonstrate the fabrication of microscale copper structures, including straight, inclined, helical, and their combined or arrayed geometries. Our experimental studies indicate that accurately estimating layer thickness through current measurement is challenging, and we also provide the first evidence that nanotwins can form in structures deposited using this voxelated MCED technique. This discovery extends the advantages of continuous pulsed voltage MCED to voxelated MCED, enhancing its potential for advanced applications involving more complex structures with enhanced mechanical properties.

2. Results and discussion

2.1. Printing principle

The schematic in figure 1(a) shows the setup of our voxel MCED system, which contains a micropipette filled with electrolyte positioned above a conductive substrate, both in a humidity-controlled environment. Precise micropipette movements are enabled by an XYZ nanopositioning stage, augmented by an XYZ coarse stage for larger substrate adjustments. The current amplifier provides instant ionic current feedback to a control unit based on a field-programmable gate array (FPGA). This unit adjusts the voltage between the anode and cathode and manages the movement of the micropipette during the printing process. In this process (figure 1(b)), the micropipette approaches the substrate until a spike of ionic current indicates contact. Subsequently, upon the formation of a meniscus, a bias voltage is applied to initiate the deposition.

The voltage drives the cations in the electrolyte to migrate towards the meniscus and get reduced, creating a metal voxel on the conductive substrate. After completing a voxel, the micropipette is withdrawn to break the meniscus and reoriented to the next deposition site according to the designed structure.

In voxelated MCED for 3D printing, the precise placement of each voxel is crucial for the formation of the intended structure. The conventional voxelated MCED process involves a sequence of steps for each voxel: first completing its deposition, then vertically retracting the micropipette, horizontally moving it to a predetermined position above the next voxel location with a biased distance Δx_i , and finally vertically approaching the substrate for the subsequent deposition. This process is illustrated by the movement trajectory of the micropipette to fabricate tilted features in figure 1(c). In an ideal scenario, if every voxel possesses uniform thickness, the biased distance between each deposition would be constant, thereby establishing a consistent tilt angle α .

However, due to the variability in experimental factors such as humidity, temperature, electrical noise, and meniscus formation state, it is challenging to ensure uniform thickness for each voxel. Therefore, positioning the next voxel based solely on a constant biased distance Δx_0 can introduce deviations. Even using the ionic current magnitude to estimate the voxel thickness according to Faraday's law may not yield accurate measurements [39], leading to errors in adjusting the subsequent positioning biased distance Δx_i .

These errors can cause the deposited structure to diverge from the originally intended design. This is demonstrated by the misalignment of the line connecting the voxel centers with the preset tilt angle in figure 1(c). The conventional approach adheres to a standard 3D printing method of vertical withdrawal, horizontal displacement, and vertical contact. This necessitates that the position of each subsequent voxel be determined based on the thickness and placement of the preceding one. Consequently, errors in estimating the thickness and position of the voxels can impact the final printed structure.

To address these challenges, we propose the self-adjusting voxelated MCED method. Unlike conventional methods that focus on the thickness of each deposited voxel and the necessary biased distance (Δx_i) based on it, our approach concentrates on aligning the micropipette's movement trajectory with the intended final structure of the print. As demonstrated in figure 1(d), the micropipette follows the trajectory of the desired structure (indicated by the red line in figure 1(d)), deposits material, and then vertically retracts, realigning itself back to the deposition pathway. This ensures that each voxel is precisely deposited along the predetermined path, regardless of any variations in voxel thickness, aligning accurately with the initially planned structure. In other words, instead of calculating Δx_i for each voxel position, our method ensures each voxel is located directly on the intended trajectory, resulting in a self-regulation of the voxel positioning.

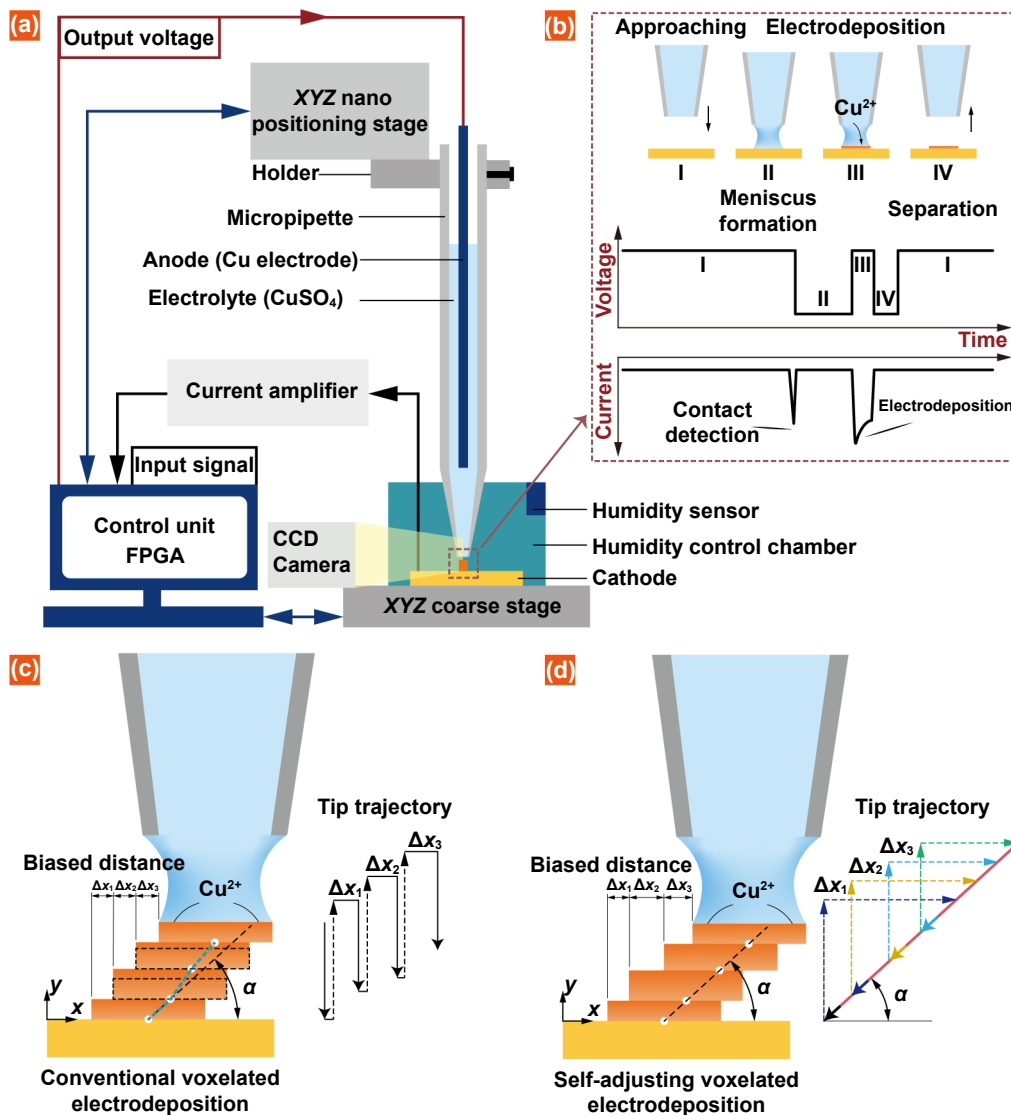


Figure 1. Principle of self-adjusting voxelated MCED method. (a) Schematic of the self-adjusting voxelated MCED setup. The setup includes a micropipette filled with electrolyte, a conductive substrate, linear platforms for coarse and precise positioning, a control unit (FPGA), and a sideview vision system. (b) Schematic of input and output signals during the printing process of a voxel. The ionic current is amplified and used as an input to the FPGA for real-time adjustment of the voltage between anode and cathode. (c) Schematic of conventional voxelated electrodeposition for tilted features with variable voxel thickness due to experimental conditions and estimated biased distance. (d) Schematic of self-adjusting voxelated electrodeposition for tilted features with adjustable biased distance to ensure the precision of the deposition.

2.2. Self-adjusting voxelated metallic structures fabrication

The fabrication process of metallic structures using the self-adjusting voxelated MCED method, exemplified by the manufacturing of helical structure arrays, is illustrated in figure 2. The fabrication process involves a patterned deposition of individual voxels, where each helical structure receives a voxel in turn. This pattern repeats, sequentially adding voxels to each structure in a series—first to helix 1, then to helix 2, followed by helix 3, and back to helix 1, and so on. This cyclical process continues until the array of three parallel helical structures is fully constructed, as depicted in figures 2(a) and (b).

In the process of depositing a single voxel, the micropipette is initially set on a specific trajectory. As it moves along

this path, the electrolyte at the tip of the micropipette comes into contact with the substrate, forming a meniscus. During this movement, the motion direction of the micropipette's tip is continuously aligned with the tangential direction of the initial trajectory, as illustrated in the first and second steps of figure 2(c). Upon this contact, a pulsed current is detected, reaching a predetermined threshold. To prevent further electrochemical reactions and avoid clogging of the micropipette, a reverse voltage is applied between the cathode and anode. This halts the reaction until a stable meniscus is formed. This stage includes a post-contact retraction of the tip by 200 nm–500 nm to ensure this stability (figure 2(c-iii)). Subsequently, a voxel is formed on the substrate after a brief period of deposition. To terminate the deposition, the

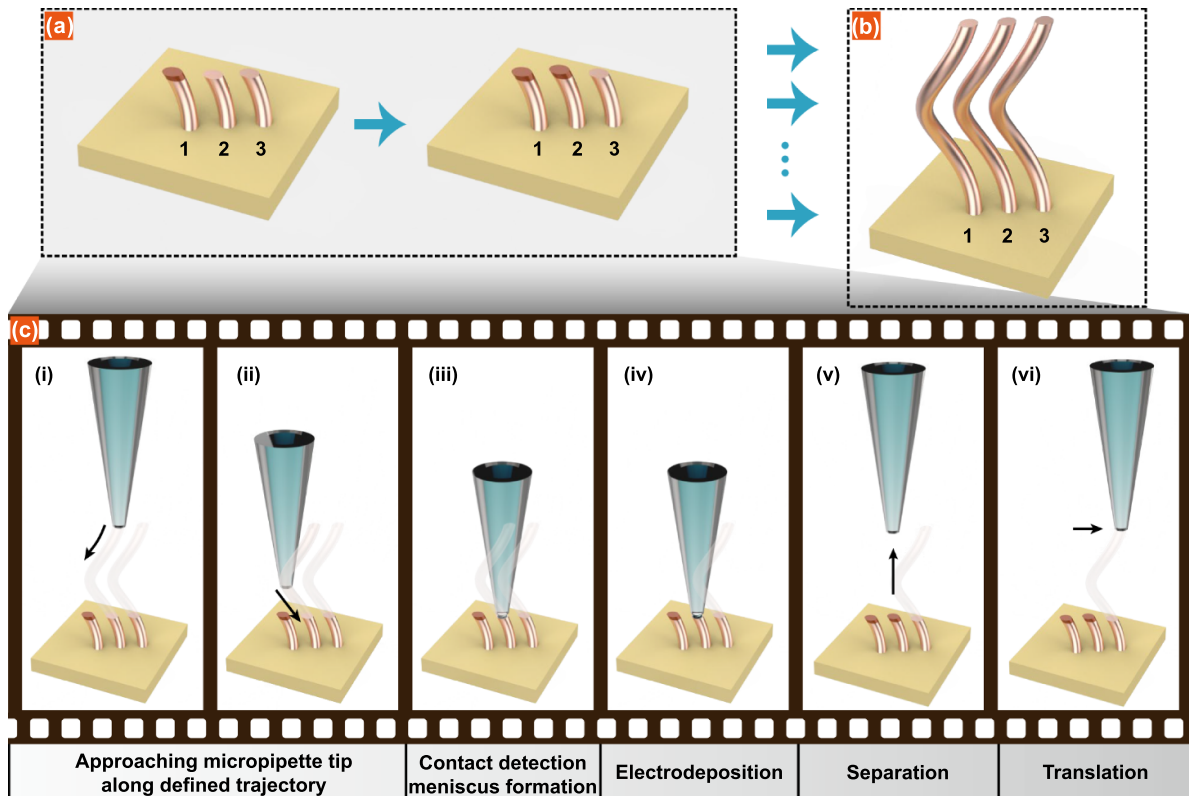


Figure 2. Parallel fabrication process of helical structures using the self-adjusting voxelated MCED method. (a) Deposition sequence. (b) The completed helical structures, produced by sequentially depositing voxels in a cyclical manner, starting with helical structure 1, then proceeding to 2 and 3, and repeating this sequence as depicted in (a). (c) The detailed procedure for the deposition of a single voxel within the second helical structure by the self-adjusting voxelated MCED method.

reverse voltage is applied again, and the micropipette is carefully detached from the substrate in a specified direction, as depicted in figure 2(c-v). Finally, the substrate is moved to the next planned position for the fabrication of the helical structure, repeating the steps described above, as shown in the last step of figure 2(c-vi).

The initial trajectory, representing the desired deposited structure and the motion path of the micropipette, is formulated as a function in an xyz coordinate system. It is discretized by scattering it over specific steps, converting the continuous path into discrete points. After each deposition, the micropipette retracts to break the meniscus. For complex structures, the substrate's separation from the nozzle is executed vertically to avoid any collision with the already deposited structure. The micropipette then automatically realigns with the planned trajectory, continuing its movement until the next contact. This cycle repeats until the entire structure is printed.

Figure 3 showcases a series of microstructures fabricated via the self-adjusting voxelated MCED method. Figures 3(a) and (b) illustrate a helical array, with each helix reaching a height of $25 \mu\text{m}$, a radius of $2.5 \mu\text{m}$, and a pitch of $25 \mu\text{m}$, as viewed from both front and top perspectives. The top view shows the overlapping projections of the structures, highlighting a complexity unattainable through conventional continuous electrochemical deposition, where

depositing one structure after another can result in interference (also evident from figure 2(c-iii)). These results demonstrate the precise control afforded by the self-adjusting voxelated MCED method in fabricating complex array and helical structures. Figure 3(c) displays structures at various tilt angles, with the actual measurements aligning closely with the targeted angles. Figure 3(d) presents an array organized in a 3×3 grid, with a uniform tilt angle of 30 degrees and side spacing of $6 \mu\text{m}$. In figure 3(e), the array is presented with each unit composed of a few voxels, featuring a size to edge-to-edge spacing ratio of approximately 6.4, evidencing the capability of our fabrication process to achieve highly dense packing of the microstructures. The characters 'H', 'I', and 'T', shown in figure 3(f), demonstrate the method's effectiveness in creating lateral structures. Altogether, these structures illustrate the method's capability for accurate deposition on curves, inclines, overhangs, and in array formations.

2.3. Characterization of metallic microstructures

The sequence of voltage application during the printing process is depicted in figure 4(a). The pulsed nature of the deposition current, due to the intermittent contact between the nozzle and substrate, not only mitigates concentration polarization by allowing time for ion replenishment but also facilitates high current density that suppresses the hydrogen evolution

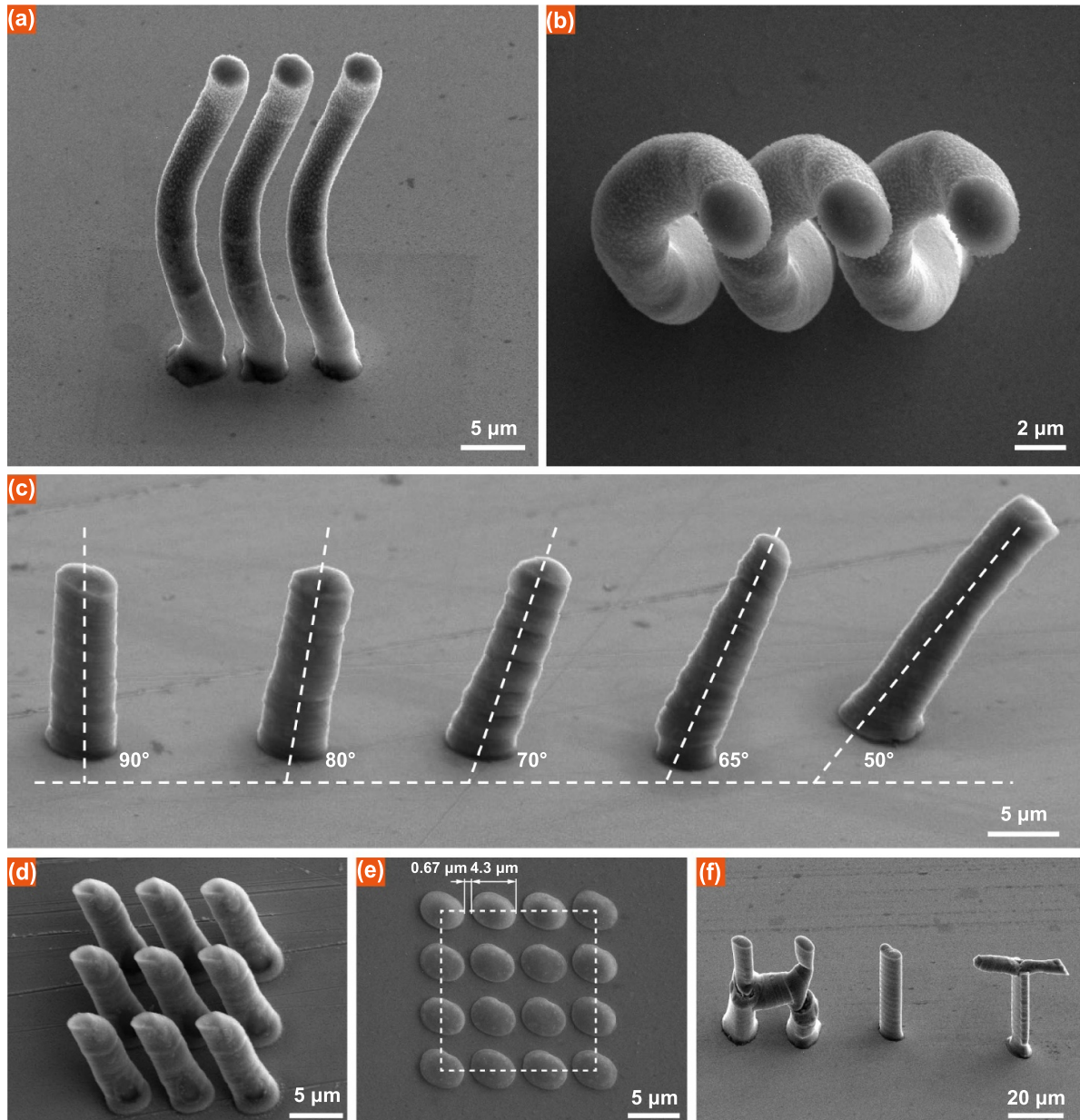


Figure 3. SEM images of microstructures fabricated using self-adjusting voxelated MCED. (a) Side view of an array of three helical structures, each with a diameter of $2.5 \mu\text{m}$, a pitch of $25 \mu\text{m}$, and an array spacing of $5 \mu\text{m}$. (b) Top view of the helix array. (c) Structures with varying tilt angles: 90° , 80° , 70° , 65° , 50° . (d) A 3×3 array of tilted structures, uniformly set at a 30° angle. (e) A 4×4 voxel array, top view. (f) The letters 'H', 'I', and 'T', printed using this method.

reaction [40]. This allows for a higher reduction voltage of 1 V, enabling the formation of dense structures without porosity, as evidenced by the experimental results (like figure 7(c)).

As the micropipette approaches the substrate, the current increases due to the formation of the meniscus. Once the current exceeds a predefined threshold, the voltage is adjusted to -0.2 V , a transition that corresponds to the formation of a stable meniscus (stage b). After this, the voltage is reverted to 1 V for a designated duration to deposit copper (stage c). At the conclusion of voxel printing (stage d), the voltage is set back to -0.2 V . Subsequently, the micropipette is withdrawn, breaking the meniscus and leading to the disappearance of the current

(returning to stage a). These stages are in alignment with the changes in ionic current observed in figure 4(b). The peak duration of the current differs with varying deposition times, as illustrated in figures 4(b-i) and (b-ii). Furthermore, even when the deposition time for voxels is identical, variations in peak current can be observed, as shown in figure S1. These variations in instantaneous current at each stage of deposition contribute to inconsistencies in voxel thickness. The red dashed line in the figure represents the current threshold, set here at 100 nA. In our self-adjusting voxelated MCED method, there is no need to estimate voxel thickness based on ionic current measurements during deposition. Instead, the ionic current primarily serves as an indicator for detecting contact between

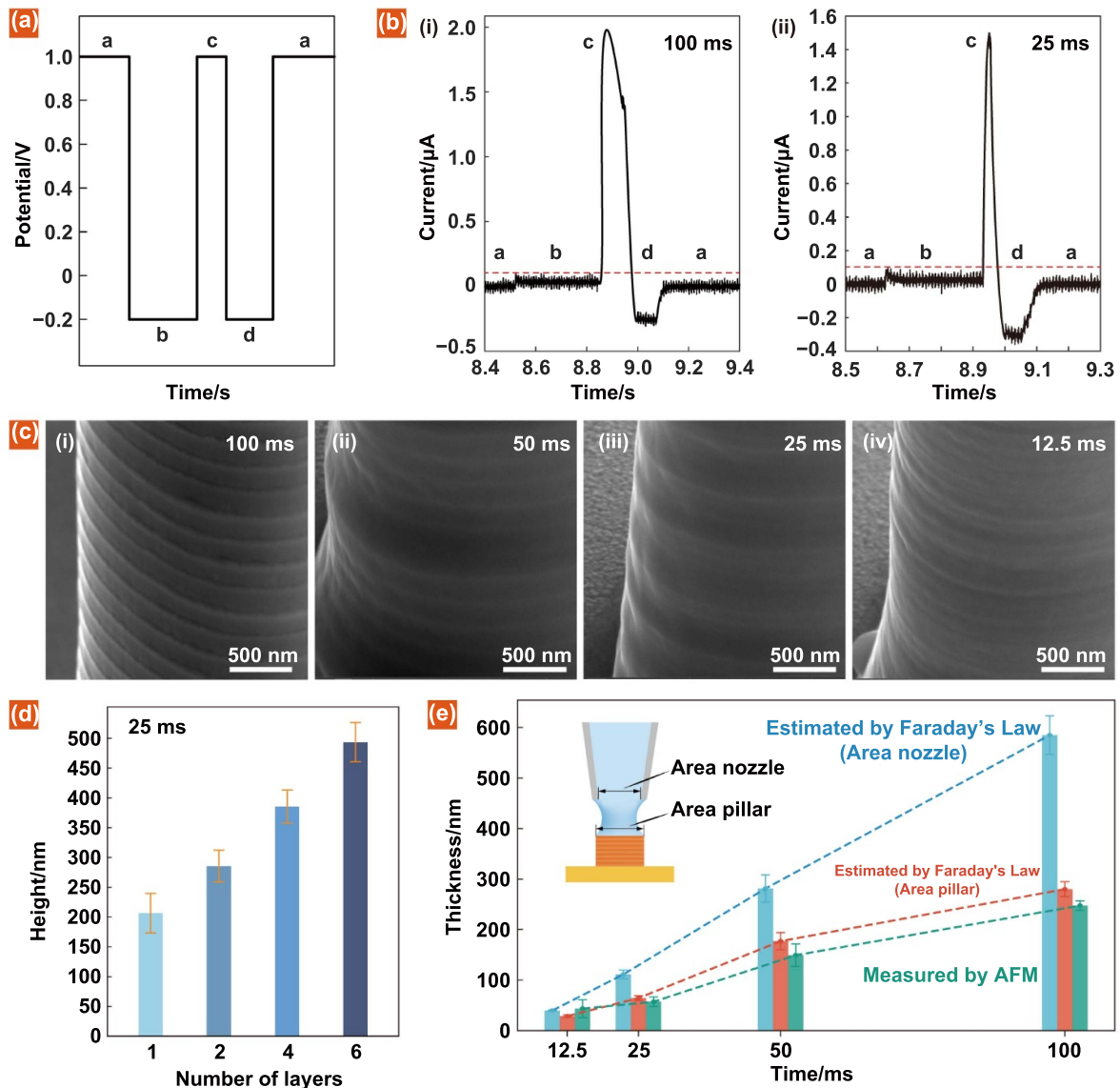


Figure 4. Time control in electrochemical deposition processes and voxel thickness analysis. (a) Voltage profile for a single voxel deposition, with 'a' to 'd' indicating the specific stages of the process that correspond to the deposition steps (i) to (iv) in figure 1(b). (b) Ionic currents for a single voxel were recorded at various deposition times, specifically at (i) 100 ms and (ii) 25 ms, with the threshold of 100 nA marked. (c) Surface morphology of deposited structures was characterized at several deposition intervals: (i) 100 ms, (ii) 50 ms, (iii) 25 ms, and (iv) 12.5 ms, with the threshold of 500 pA. (d) Height variation of micropillars across different deposition layers, with each layer deposited for 25 ms. (e) Voxel thickness variation with deposition time as indicated by measurements via AFM (green bars) compared with thickness estimated using the nozzle area (blue bars) and the actual pillar area (red bars) according to Faraday's law. The dashed lines indicate the positive correlation between voxel thickness and deposition time. The inset shows the areas used for estimation in electrodeposition setup.

the micropipette and the substrate. To enhance sensitivity in practical applications, we increased the amplifier's gain and set the current threshold at 500 pA. Although the peak deposition current exceeds the amplifier's range at this gain setting, this approach is beneficial for facilitating more precise contact detection.

To further quantify the relationship between single voxel deposition time and deposition thickness, we examined vertical structures with varying deposition times to investigate the impact of deposition duration on structural morphology and voxel thickness. Figure 4(c) displays the surface morphology

of structures at deposition times of 100 ms, 50 ms, 25 ms, and 12.5 ms. It is observed that with decreasing deposition time, the layering of the printed structure becomes less distinct, and the surface morphology appears smoother, albeit at the expense of increased printing times.

Following this analysis, we further evaluated the accuracy of Faraday's law in estimating voxel heights under varied deposition durations. Micropillar arrays with 1, 2, 4, and 6 layers were characterized using AFM to obtain their topography (figure S2). The first layer exhibited greater thickness compared to subsequent layers, as shown in figure 4(d).

This discrepancy arises due to the initial layer being deposited on the Au substrate, in contrast to subsequent layers which are deposited on Cu. Thus, the average thickness of layers for different deposition times was calculated by subtracting the thickness of the first layer from the total thickness of the stacked layers, as indicated by the green bars in figure 4(e). Estimations of deposition thickness using Faraday's law require knowledge of both the cross-sectional area of the micropillars and the total charge transfer during deposition, which is the integral of the current over time. Figure 4(e) illustrates the comparison between thickness estimates using both the nozzle and actual pillar areas against the actual AFM measurements. Although the trends align, notable differences exist between the estimated and actual values, particularly when estimating using the nozzle area, which at 100 ms can exceed the actual values by over twice (as shown by the blue and green bars). In contrast, estimates using the actual pillar area closely match the AFM measurements (red and green bars). Table S2 highlights the discrepancies in the actual areas of pillars at different deposition durations. These discrepancies are likely a result of environmental and process-related factors. Changes in ambient humidity, temperature fluctuations, and variations in the position where the nozzle contacts the substrate can all alter the meniscus shape formed during each voxel deposition, leading to variations in the deposited area. Notably, such variations in the meniscus shape are not limited to vertical structures but can also occur in tilted, lateral, and curved structures. In these cases, the non-parallel orientation of the growth front relative to the pipette tip can cause adaptive changes in the meniscus shape, potentially amplifying the variations in the deposited area. Currently, accurately determining the deposition area during the process is a challenge, making the use of this area for estimating the quantity of deposited metal nearly impossible.

Moreover, analysis of AFM topography images has determined the actual layer thickness of copper pillars under the conditions of 1 V voltage and $0.6 \text{ mol}\cdot\text{l}^{-1}$ electrolyte concentration (table S3), which achieves a growth rate of approximately $2.82 \mu\text{m}\cdot\text{s}^{-1}$ (table S4). Our method significantly outperforms reported traditional direct current, pulsed, and voxel MCED techniques in terms of deposition speed and volume rate (table S5). This is due to the use of higher voltages and electrolyte concentrations, which results in higher current density and deposition volume rate without compromising the deposition surface quality. The comprehensive printing speed of our method, considering both deposition speed and necessary nozzle movements, is approximately $10.8 \text{ nm}\cdot\text{s}^{-1}$, comparable to existing techniques [31, 32]. However, optimizing the control methods could reduce the time required for nozzle movements, further enhancing the overall printing speed and taking full advantage of the high deposition speed of our approach. Our printing resolution is currently limited by the nozzle diameter ($\sim 3 \mu\text{m}$) and the precision of our nanopositioning stage (1 nm). Employing smaller nozzles and higher-precision positioning stages has the potential to significantly improve the printing resolution, enabling the fabrication of nanoscale features.

To showcase the versatility of the self-adjusting voxelated MCED technique, we fabricated a series of structures with varying tilt angles. As shown in figure 3(c), the structures were deposited at angles of 90° , 80° , 70° , 65° , and 50° relative to the horizontal axis. The process parameters for deposition were set to an applied voltage of 1 V, a current threshold of 500 pA, with each voxel deposited over a period of 25 ms. Figure 5(a) illustrates the development of a structure at a 70° tilt, where the micropipette's motion—approaching and retracting from the substrate—is governed by the angle of deposition, facilitating a voxel formation upon contact and then detaching at either the same inclined angle or vertically. This method ensures the micropipette's trajectory is always tangent to the growth path, enabling a self-adaptive deposition. Altering parameters such as the deposition time or the applied voltage can adjust the voxel thickness while leaving the structure's final angle unaffected. As depicted in figure 5(c), the deposition surface maintains a perpendicular orientation to the growth direction at all times. Horizontal structures are achieved through a process of horizontal contact and subsequent separation, as shown in figures 5(d)–(f). The horizontal segments of the letter 'H' are printed layer by layer using this horizontal approach (figure 5(e)), as demonstrated in figure 5(d). In the lateral deposition of these structures, the deposition plane is maintained perpendicular to the growth direction, consistent with the formation of the tilted structures, as evidenced in figure 5(f).

Transmission electron microscopy (TEM) was utilized to characterize the cross-section of the copper pillar printed using the voxelated electrochemical deposition method. Prepared at 1 V with a deposition time of 25 ms, the sample was thinned to 100 nm using FIB milling. High-resolution imaging was then conducted with a Talos F200X TEM operating at 200 keV. In figure 6, the longitudinal section of the deposited copper pillar is displayed, showing that the transverse structures have nanotwins. A low magnification view of the sample in figure 6(a) includes an inset of the selected area diffraction pattern (SADP), highlighting many differently oriented crystallites. An enhanced view of nanotwins, which align with the grain growth direction, is featured in figure 6(b). The distribution of twin lamella thickness is presented in a histogram in figure 6(c), with an average thickness around 8.5 nm. High-resolution TEM images in figures 6(d)–(f) reveal the lattice planes, with the inset SADP in figure 6(d) confirming the twinning with its characteristic double-spot pattern. The intersection of twin boundaries (TB) and grain boundaries (GB) on the plane is evident in figure 6(e). Lastly, figure 6(f) details the symmetrical lattice orientation around a TB, where mirrored dashed lines illustrate the symmetry, and variations in d-spacing are consistent with (111) planes, further elaborated in figure S3.

The ability of the self-adjusting voxelated deposition process to generate nanotwins can be attributed to the short intervals of meniscus contact between the micropipette and the substrate. During these brief contact periods, a high current density is achieved, similar to the 'on' phases in pulsed electrodeposition (PED) [31–33]. This leads to a rapid

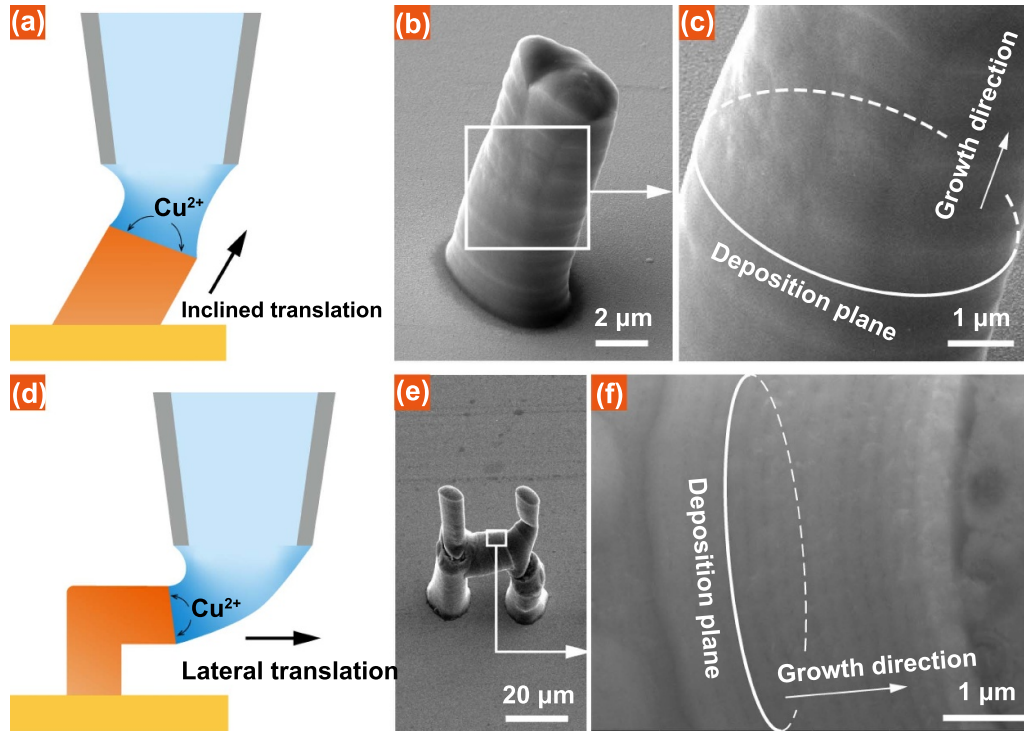


Figure 5. Printed tilted and lateral structures. (a) Schematic diagram of deposition principle of a tilted structure. (b) SEM image of the microstructure with a tilt angle of 70° . (c) Close-up view of the microstructure in (b), highlighting the deposition plane and growth direction. (d) Schematic diagram of deposition principle of a lateral structure. (e) SEM image of the printed letter ‘H’. (f) Zoomed-in SEM image of the lateral structure in (e), showing the deposition plane and direction of growth.

deposition rate and an increased density of nucleation sites, which are favorable for nanotwins formation. After each deposition period, the retraction of the micropipette interrupts the grain growth, allowing for the relaxation and renucleation of the deposited ions. This interruption is crucial for replenishing the metal ions in the diffusion layer, thereby maintaining a high peak current density at the cathode ($\sim 9.5 \text{ A}\cdot\text{cm}^{-2}$). Thus, the intermittent contact inherent in the voxelated deposition process mirrors the effects of t_{off} observed in PED, playing a key role in the emergence of nanotwins by allowing for ion relaxation and maintaining a high ion concentration within the meniscus [31].

Interestingly, even though we used a layer-by-layer deposition method to print the copper pillar, no significant delamination was observed at the interfaces, as shown in figure 7. Despite not deliberately controlling the thickness of each deposited layer, we estimated the thickness of a voxel (deposited over a period of 25 ms) to be between 45 nm and 70 nm based on figure 4(e). In figure 7(a), the low magnification TEM images reveal no noticeable interlayer within the observed field. Furthermore, the high magnification TEM images in figure 7(b), marked with arrows, show that some regions containing nanotwins exceed 200 nm, far larger than the thickness of a single deposited layer, suggesting continuous grain growth. The energy dispersive x-ray spectroscopy (EDS) analysis in figure S4 confirms the high purity of copper. Figure 7(c), after FIB milling, shows areas selected for the EDS analysis, and the EDS maps in figures 7(d) and (e)

indicate continuous copper distribution without oxygen interlayers, implying that the voxelated deposition does not compromise the mechanical and electrical properties of the structure by creating delamination interfaces.

Nanotwins produced by voxelated deposition share similarities with those obtained from PED. In both techniques, high current densities are achieved rapidly, and ion concentrations are replenished during the non-deposition phases. The key difference lies in the meniscus dynamics: PED maintains continuous contact between the nozzle and the substrate, keeping the meniscus constant even in ‘off’ periods. In contrast, voxelated deposition involves intermittent contact, repeatedly forming and breaking the meniscus. Despite this difference, voxelated deposition upholds structural integrity comparable to PED, as demonstrated by TEM and EDS analyses in figure 7. The advantages of voxelated deposition include minimizing the risk of micropipette clogging, allowing the use of higher voltages and electrolyte concentrations, and offering the capability to create complex patterns and arrays. These features collectively enhance the flexibility in designing printed structures.

Grain refinement is known to result in the hardening of materials, including metals and alloys. This phenomenon is described by the empirical Hall-Petch relation at the micron to submicron scale, which states that material strength is inversely proportional to grain size [41, 42]. GB enhance material strength by impeding the glide of dislocations, with a reduction in grain size leading to an increased

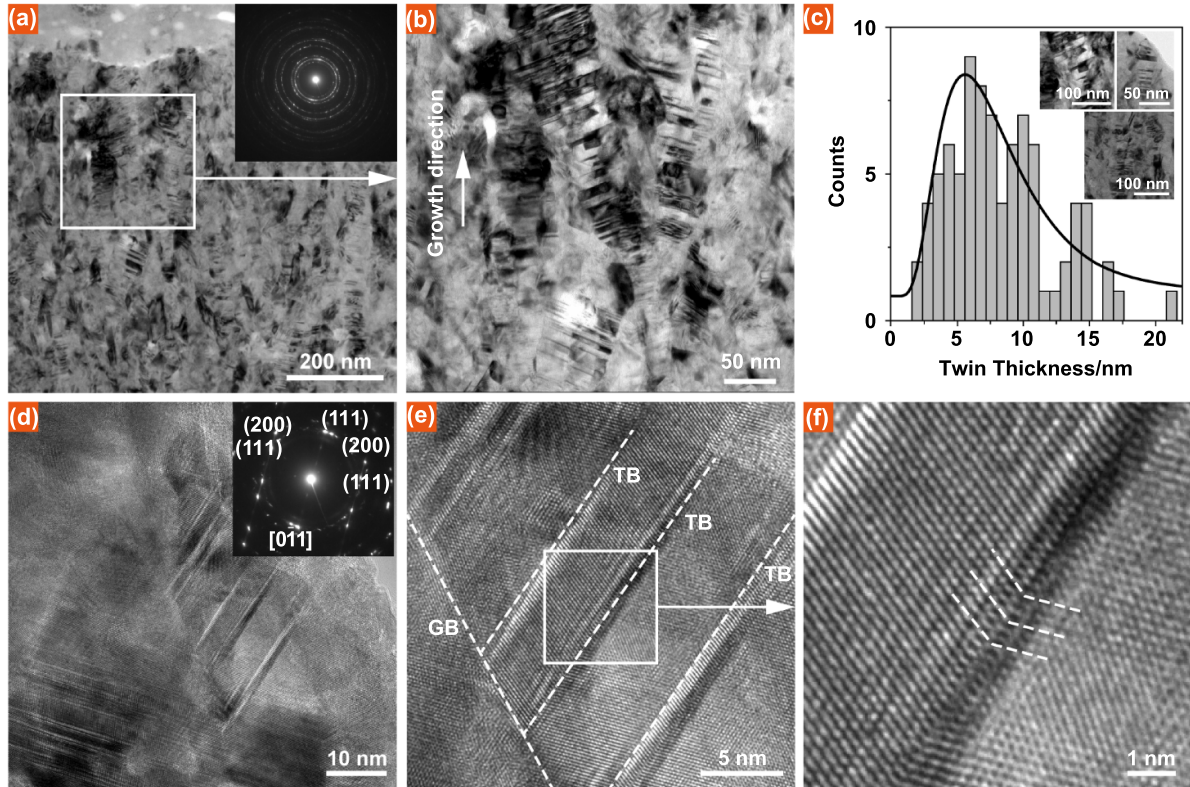


Figure 6. TEM images of structures deposited by self-adjusting voxelated MCED method. (a) Low magnification view shows a dense population of nanoscale grains, with the SADP inset indicating their crystalline orientations. (b) Localized nanotwins along the growth direction. (c) Histogram of twin lamella thickness with an average value of 8.5 nm. (d) High-resolution imaging of lattice planes, with SADP inset confirming the double-spot diffraction patterns. (e) Intersection of twin boundaries (TB) and grain boundaries (GB). (f) Symmetrical lattice orientation of nanotwins.

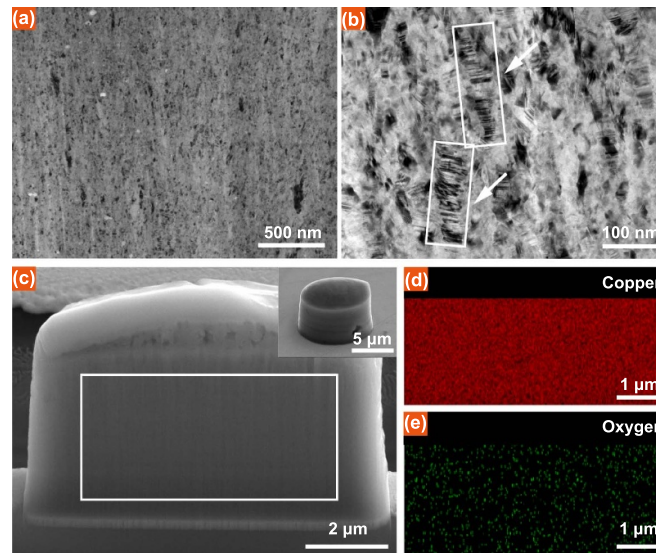


Figure 7. Microstructure and elemental analysis of the deposited copper pillar. (a) TEM image at low magnification showing the cross-section of the copper pillar with no visible interlayer structures. (b) High magnification TEM image revealing nanotwins; in some regions, these nanotwins are observed to be thicker than the average layer thickness. (c) SEM image displaying the sample after FIB milling for cross-sectional analysis, with an inset depicting the structure prior to milling. (d) and (e) EDS maps of copper and oxygen, respectively, corresponding to the milled area highlighted in (c), showcasing the elemental distribution.

grain boundary area that further impedes dislocation motion. Similarly, TB, akin to conventional GB, obstruct dislocation motion, contributing to material strength [43, 44]. In

the case of electrodeposited copper, the formation of nanotwins plays a crucial role in enhancing its mechanical properties.

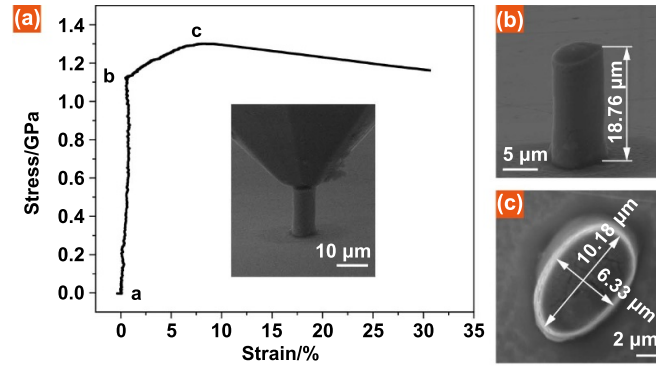


Figure 8. *In-situ* SEM microcompression experiment on voxelated copper pillar. (a) Stress–strain curve of a voxelated copper pillar during *in-situ* SEM microcompression testing, with an inset showing the copper pillar and indenter at the point of contact. (b) Initial SEM image of the copper pillar before compression, showing the height measurements. (c) SEM image of the undeformed top area of the copper pillar, displaying the area dimensions.

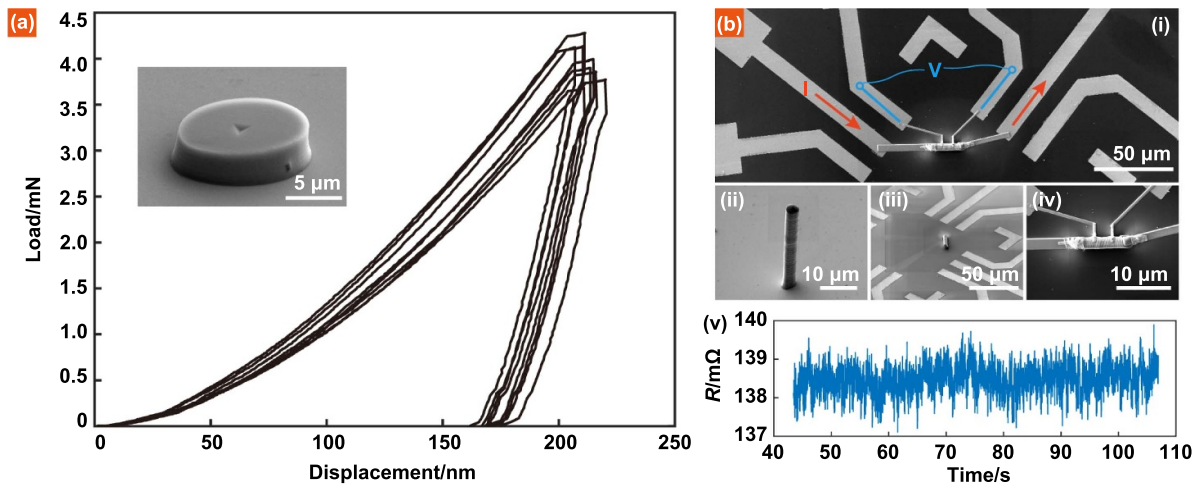


Figure 9. Hardness and resistivity measurements of the deposited Cu pillars. (a) Load–displacement curves for the indentation tests performed on eight micropillars, with an inset showing a representative indented micropillar. (b) Experimental setup and results for Cu micropillar resistivity measurements. (b-i) illustrates the overall setup used for electrical resistivity measurements, known as the four-point probe method. Detailed views in (b-ii) and (b-iii) show the micropillar before and after separation from the substrate, respectively. In (b-iv), the micropillar is shown mounted on the resistance testing chip, with the FIBID technique applied to connect it to the chip's terminals. The electrical resistance over time for the micropillar is captured in (b-v).

The printing direction can potentially affect the orientation of nanotwins in the electrodeposited copper due to changes in the meniscus shape and the resulting growth direction (figure 5). While the nanotwins orientation may affect the strain rate sensitivity, its impact on the overall hardness is expected to be limited [45]. The formation of nanotwins, regardless of their orientation, is the primary factor contributing to the enhanced mechanical properties of the electrodeposited copper.

In-situ SEM microcompression experiments on the voxelated deposition copper pillar (figures 8(b) and (c)), as described in the SI (figure S5), revealed a compressive yield strength of 1.1 GPa at point b and an ultimate strength of 1.3 GPa at point c (figure 8(a)). The yield strength slightly exceeds those from PED (962 ± 26 MPa) and is significantly higher than DC electrodeposition (656 ± 46 MPa) [32]. The indentation tests, as illustrated in figure 9(a), provided an

average hardness of 3.71 GPa for the pillars, with a maximum value reaching 4.27 GPa. This hardness is significantly greater than that observed in copper devoid of nanotwins, typically ranging between 1.4 GPa and 1.6 GPa, and surpasses even copper with a high density of nanotwins, which has been previously reported to possess hardness values between 2.0 GPa and 2.6 GPa [46]. These results, demonstrating superior mechanical properties, can be attributed to the dynamic meniscus formation and breakage during the voxelated deposition process. This mechanism leads to the formation of smaller nanotwins, consequently enhancing structural strength and hardness. TEM observations provide corroborating evidence, confirming the presence of these nanotwin structures within the material. The electrical properties of the deposited structure were evaluated by employing FIB milling to separate the micropillars from their substrate (figure 9(b-ii)) and transferring them to a resistance testing chip (figure 9(b-iii)). FIBID

was used to connect both ends and the central measuring point of the micropillars to corresponding pins on the chip (figure 9(b-iv)). A four-point probe method (figure 9(b-i)) was employed to measure a mid-section resistance of 138.5 m Ω . The resistivity of the deposited structures was determined to be approximately $(1.95 \pm 0.01) \times 10^{-7} \Omega\cdot\text{m}$, nearly 11 times that of bulk copper ($(1.69 \times 10^{-8}) \Omega\cdot\text{m}$) about half that of the pulsed MCED method [31].

The increased resistivity observed in the deposited structures, compared to bulk copper and larger-scale nanotwin structures [33], is hypothesized to be due to the micron scale of the sample length and cross-sectional area. This leads to significant Joule heating, which elevates the resistivity measurements. Despite the increase in resistivity, this analysis indicates that while mechanical properties can be significantly enhanced through the introduction of nanotwins, conductivity does not drastically decrease. Table S6 compares the electrical conductivity, hardness, and yield strength of structures fabricated by various advanced methods. The analysis of structures fabricated by our method indicates that while the introduction of nanotwins by our method can significantly enhance strength, it does not drastically decrease conductivity. This finding offers a promising avenue for optimizing material properties in microscale printed metallic structures, such as microsensors, microelectronics, and micro-electromechanical systems (see SI section 9 for details).

3. Conclusion

In summary, this study introduces a novel self-adjusting voxelated MCED method for the precision 3D printing of metallic microstructures. By focusing on aligning the micropipette's trajectory with the intended final structure, rather than relying on the thickness of each voxel, our approach elegantly improves the accuracy and reliability of the printing process. This method effectively overcomes the challenges posed by variability in experimental factors, such as humidity and temperature, which previously led to inconsistencies in voxel thickness and misalignments in the deposited structure. The fabrication of intricate helical structures and arrays with varying tilt angles demonstrates the method's capability to precisely control deposition along desired trajectories, ensuring accurate realization of complex designs. The presence of nanotwins in the structure was confirmed by TEM analysis, and extremely high strength and hardness as well as low resistivity were obtained. This advancement further emphasizes its potential in material science, offering new possibilities for developing microstructures with enhanced mechanical and electrical properties. Our self-adjusting voxelated MCED method advances the fabrication of metallic microstructures, enabling more accurate, diverse, and improved performance structures, beneficial for micro-electromechanical systems and other applications.

4. Experimental section

4.1. Micropipette

The micropipette was fabricated using a commercial laser-based micropipette puller (P-2000, Sutter Instruments). We produced nozzles with different opening areas, pulled from borosilicate glass tubing of 1.2 mm outer diameter and 0.9 mm inner diameter (TF120F-6, WPI). Details of the pulling process are showcased in figure S6, and the specific parameters used are provided in the supporting information, table S7.

4.2. Electrochemical printing setup

The electrochemical printing system depicted in figure 1 comprises a glass nozzle (micropipette), a conductive substrate, a high-precision motion stage, a microscopic vision system, and a control unit. The micropipette, filled with 0.6 M $\text{CuSO}_4 \cdot 5\text{H}_2\text{O}$ electrolyte, houses a copper wire anode, while a gold-plated substrate serves as the cathode. Coarse positioning of the substrate, the CCD camera (acA2040-120uc, Basler), and the micropipette holder is independently achieved by their respective xyz -axis coarse positioning stages (LD-60, SELN). Precise micropipette positioning utilizes a linear piezo nanopositioning system (SLC-1720, Smaract) with sub-nanometer resolution. A current amplifier (DLPCA-200, Femto) connected to the substrate acts as an ammeter. An FPGA card-equipped computer (PXI-7852R, National Instruments) with a LABVIEW program controls input signal acquisition and voltage output. During deposition, a controllable bias voltage from the FPGA card is applied between the copper wire and substrate. The current amplifier, with a gain setting of 10^9 , enhances the signal for accurate detection and feeds this amplified signal to the data acquisition card. Initial settings include a 1 V bias voltage and a 500 pA current threshold.

When the nanostage controls the micropipette's tip to approach the substrate, the forward step distance is 100 nm. The electrolyte inside the micropipette's tip is slightly higher than the edge of the pipette due to surface tension. Once the micropipette contacts the gold-plated substrate, a meniscus is formed between the internal electrolyte and the substrate. Upon threshold exceedance, a -0.2 V reverse voltage is applied, and the micropipette retracts from the substrate by 200–500 nm (200 nm for deposition times less than 25 ms, and 500 nm for deposition times greater than 25 ms). This retraction distance is less than 1/4 of the pipette's diameter (a meniscus less than 1/2 of the pipette's diameter can maintain stability) and is also higher than the deposited voxel layer thickness at different times, as shown in table S3. Therefore, the meniscus can remain stable during the deposition process without causing clogging of the pipette. Finally, the voltage is reset to 1 V. This process, crucial for avoiding nozzle clogging, is precisely managed by the FPGA-equipped computer.

The printing area, including the substrate and micropipette nozzle, is enclosed in a transparent, humidity-controlled

chamber. Humidity is regulated using a water vapor generator and monitored with a humidity sensor (DHT22, HAIGU), maintaining levels between 55%–60%. The chamber is equipped with glass viewing windows on two sides for microscopic observation. Furthermore, the entire deposition system is encased in a Faraday cage to eliminate electromagnetic interference from external devices, ensuring the accuracy of the electrochemical printing process.

4.3. Characterization and instruments

The morphology of the metal deposits was analyzed using a dual beam FIB scanning electron microscopy system (FIB-SEM, TESCAN AMBER). EDS analyses and TEM sample preparation were also performed using this equipment. The microscopic nanotwin grains in the deposited metals were analyzed via TEM (Talos F200X, Thermo Scientific).

The strength of the deposited metal structures was characterized using *in-situ* SEM microcompression experiments (Scios™ 2, Thermo Scientific). Indentation tests were conducted using a KLA (formerly Agilent, Keysight) G200 Nanoindenter to explore the impact of nanotwins on the mechanical properties of the printed structures. A manufacturer-calibrated Berkovich tip was employed to indent eight deposited micropillars. The continuous stiffness measurement technique was utilized with a constant strain rate of 0.05 s^{-1} until a depth of 200 nm was reached, and load and displacement curves were recorded.

The electrical resistivity measurement was performed using the four-point probe method with a Keithley Source Measurement Unit-2636B. The micropillar transfer process, including FIB milling and FIBID, was conducted using a dual beam FIB scanning electron microscopy system (FIB-SEM, TESCAN AMBER).

Data availability statement

The data that support the findings of this study are available from the corresponding author upon reasonable request.

Acknowledgment

The authors would like to thank Dr Yongchun Zou and Dr Shaoyuan Sun from the Center of Analysis and Measurement at Harbin Institute of Technology for preparing the samples for electrical conductivity measurements using FIB and for hardness measurements, respectively. This work was supported in part by National Key R&D Program of China under Grant 2023YFB4705600, in part by the National Natural Science Foundation of China under Grants 61925304, 62127810 and 62203138, in part by the National Postdoctoral Program for Innovative Talents under Grant BX20200107, and in part by the Self-Planned Task (No. SKLRS202205C) of State Key Laboratory of Robotics and System (HIT).

Conflict of interest

The authors declare no conflict of interest.

Author contributions

X M and X W contributed equally to this work. X M and H X conceived and designed the study. X M, X W, and X S developed the MCED system and fabricated the metallic microstructures. X W, X M, and Y X were responsible for characterizing the deposited metal structures. X M, X W, and H Z analyzed the experimental data. H X and M C provided supervision for the study. All authors contributed to writing the manuscript.

ORCID iDs

Xianghe Meng  <https://orcid.org/0000-0002-4924-4132>
 Hao Zhang  <https://orcid.org/0000-0003-1896-9859>
 Mingjun Chen  <https://orcid.org/0000-0003-2549-3713>
 Hui Xie  <https://orcid.org/0000-0003-4299-2776>

References

- [1] Maruo S, Nakamura O and Kawata S 1997 Three-dimensional microfabrication with two-photon-absorbed photopolymerization *Opt. Lett.* **22** 132–4
- [2] Fischer J and Wegener M 2013 Three-dimensional optical laser lithography beyond the diffraction limit *Laser Photon. Rev.* **7** 22–44
- [3] Gissibl T, Thiele S, Herkommer A and Giessen H 2016 Two-photon direct laser writing of ultracompact multi-lens objectives *Nat. Photon.* **10** 554–60
- [4] Frenzel T, Kadic M and Wegener M 2017 Three-dimensional mechanical metamaterials with a twist *Science* **358** 1072–4
- [5] Xu H F, Wu S, Liu Y, Wang X P, Efremov A K, Wang L, McCaskill J S, Medina-Sánchez M and Schmidt O G 2024 3D nanofabricated soft microrobots with super-compliant picoforce springs as onboard sensors and actuators *Nat. Nanotechnol.* **19** 494–503
- [6] Li W M, Huang G S, Wang J, Yu Y, Wu X J, Cui X G and Mei Y F 2012 Superelastic metal microspheres as fluidic sensors and actuators *Lab Chip* **12** 2322–8
- [7] Yi Z R, Lei Y, Zhang X Y, Chen Y N, Guo J J, Xu G J, Yu M-F and Cui P 2017 Ultralow flexural properties of copper microhelices fabricated via electrodeposition-based three-dimensional direct-writing technology *Nanoscale* **9** 12524–32
- [8] Zhou N J, Liu C Y, Lewis J A and Ham D 2017 Gigahertz electromagnetic structures via direct ink writing for radio-frequency oscillator and transmitter applications *Adv. Mater.* **29** 1605198
- [9] Yi Z R, Guo J J, Chen Y N, Zhang H Q, Zhang S, Xu G J, Yu M F and Cui P 2016 Vertical, capacitive microelectromechanical switches produced via direct writing of copper wires *Microsyst. Nanoeng.* **2** 16010
- [10] Sattelkow J, Frösch J E, Winkler R, Hummel S, Schwalb C and Plank H 2019 Three-dimensional nanothermistors for thermal probing *ACS Appl. Mater. Interfaces* **11** 22655–67
- [11] Murr L E, Gaytan S M, Ramirez D A, Martinez E, Hernandez J, Amato K N, Shindo P W, Medina F R and

- Wicker R B 2012 Metal fabrication by additive manufacturing using laser and electron beam melting technologies *J. Mater. Sci. Technol.* **28** 1–14
- [12] Winkler R, Fowlkes J D, Rack P D and Plank H 2019 3D nanoprinting via focused electron beams *J. Appl. Phys.* **125** 210901
- [13] Shimojo M, Mitsuishi K, Tanaka M, Han M and Furuya K 2004 Application of transmission electron microscopes to nanometre-sized fabrication by means of electron beam-induced deposition *J. Microsc.* **214** 76–79
- [14] Hirt L, Reiser A, Spolenak R and Zambelli T 2017 Additive manufacturing of metal structures at the micrometer scale *Adv. Mater.* **29** 1604211
- [15] Ahn B Y, Duoss E B, Motala M J, Guo X, Park S-I, Xiong Y, Yoon J, Nuzzo R G, Rogers J A and Lewis J A 2009 Omnidirectional printing of flexible, stretchable, and spanning silver microelectrodes *Science* **323** 1590–3
- [16] Skylar-Scott M A, Gunasekaran S and Lewis J A 2016 Laser-assisted direct ink writing of planar and 3D metal architectures *Proc. Natl Acad. Sci. USA* **113** 6137–42
- [17] Farahani R D, Dalir H, Le Borgne V, Gautier L A, El Khakani M A, Lévesque M and Therriault D 2012 Direct-write fabrication of freestanding nanocomposite strain sensors *Nanotechnology* **23** 085502
- [18] Park J-U et al 2007 High-resolution electrohydrodynamic jet printing *Nat. Mater.* **6** 782–9
- [19] Galliker P, Schneider J, Eghlidi H, Kress S, Sandoghdar V and Poulidakos D 2012 Direct printing of nanostructures by electrostatic autofocussing of ink nanodroplets *Nat. Commun.* **3** 890
- [20] Wang J W, Auyeung R C Y, Kim H, Charipar N A and Piqué A 2010 Three-dimensional printing of interconnects by laser direct-write of silver nanopastes *Adv. Mater.* **22** 4462–6
- [21] In't Veld B H, Overmeyer L, Schmidt M, Wegener K, Malshe A and Bartolo P 2015 Micro additive manufacturing using ultra short laser pulses *CIRP Ann.* **64** 701–24
- [22] Tanaka T, Ishikawa A and Kawata S 2006 Two-photon-induced reduction of metal ions for fabricating three-dimensional electrically conductive metallic microstructure *Appl. Phys. Lett.* **88** 081107
- [23] Nakamura R, Kinashi K, Sakai W and Tsutsumi N 2014 Fabrication of the silver structure through two-photon excitation by femtosecond laser *Chem. Phys. Lett.* **610–611** 241–5
- [24] Kuebler S M, Tal A and Chen Y S 2008 Preparation of metallo-dielectric photonic crystals by multi-photon direct laser writing *Proc. SPIE* **6901** 69010Z
- [25] Standaert A, Brancato L, Lips B, Ceyssens F, Puers R and Reynaert P 2018 Three techniques for the fabrication of high precision, mm-sized metal components based on two-photon lithography, applied for manufacturing horn antennas for THz transceivers *J. Micromech. Microeng.* **28** 035008
- [26] Gansel J K, Thiel M, Rill M S, Decker M, Bade K, Saile V, Von Freymann G, Linden S and Wegener M 2009 Gold helix photonic metamaterial as broadband circular polarizer *Science* **325** 1513–5
- [27] Zeeshan M A, Grisch R, Pellicer E, Sivaraman K M, Peyer K E, Sort J, Özkale B, Sakar M S, Nelson B J and Pané S 2014 Hybrid helical magnetic microrobots obtained by 3D template-assisted electrodeposition *Small* **10** 1284–8
- [28] Hu J and Yu M-F 2010 Meniscus-confined three-dimensional electrodeposition for direct writing of wire bonds *Science* **329** 313–6
- [29] Suryavanshi A P and Yu M-F 2007 Electrochemical fountain pen nanofabrication of vertically grown platinum nanowires *Nanotechnology* **18** 105305
- [30] Seol S K, Kim D, Lee S, Kim J H, Chang W S and Kim J T 2015 Electrodeposition-based 3D printing of metallic microarchitectures with controlled internal structures *Small* **11** 3896–902
- [31] Behroozfar A, Daryadel S, Morsali S R, Moreno S, Baniasadi M, Bernal R A and Minary-Jolandan M 2018 Microscale 3D printing of nanotwinned copper *Adv. Mater.* **30** 1705107
- [32] Daryadel S, Behroozfar A, Morsali S R, Moreno S, Baniasadi M, Bykova J, Bernal R A and Minary-Jolandan M 2018 Localized pulsed electrodeposition process for three-dimensional printing of nanotwinned metallic nanostructures *Nano Lett.* **18** 208–14
- [33] Lu L, Shen Y F, Chen X H, Qian L H and Lu K 2004 Ultrahigh strength and high electrical conductivity in copper *Science* **304** 422–6
- [34] Eliyahu D, Gileadi E, Galun E and Eliaz N 2020 Atomic force microscope-based meniscus-confined three-dimensional electrodeposition *Adv. Mater. Technol.* **5** 1900827
- [35] Hirt L, Ihle S, Pan Z J, Dorwling-Carter L, Reiser A, Wheeler J M, Spolenak R, Vörös J and Zambelli T 2016 Template-free 3D microprinting of metals using a force-controlled nanopipette for layer-by-layer electrodeposition *Adv. Mater.* **28** 2311–5
- [36] Ercolano G, Zambelli T, van Nesselroy C, Momotenko D, Vörös J, Merle T and Koelmans W W 2020 Multiscale additive manufacturing of metal microstructures *Adv. Eng. Mater.* **22** 1900961
- [37] Ren W F, Xu J K, Lian Z X, Sun X Q, Xu Z M and Yu H D 2022 Localized electrodeposition micro additive manufacturing of pure copper microstructures *Int. J. Extrem. Manuf.* **4** 015101
- [38] Lin Y-P, Zhang Y and Yu M-F 2019 Parallel process 3D metal microprinting *Adv. Mater. Technol.* **4** 1800393
- [39] Hengsteler J, Mandal B, van Nesselroy C, Lau G P S, Schlotter T, Zambelli T and Momotenko D 2021 Bringing electrochemical three-dimensional printing to the nanoscale *Nano Lett.* **21** 9093–101
- [40] Zhang X R, Zhang X Y, Liu Z H, Tao C Y and Quan X J 2019 Pulse current electrodeposition of manganese metal from sulfate solution *J. Environ. Chem. Eng.* **7** 103010
- [41] Hall E O 1951 The deformation and ageing of mild steel: III discussion of results *Proc. Phys. Soc. B* **64** 747–53
- [42] Lu K 2016 Stabilizing nanostructures in metals using grain and twin boundary architectures *Nat. Rev. Mater.* **1** 16019
- [43] Lu L, Chen X, Huang X and Lu K 2009 Revealing the maximum strength in nanotwinned copper *Science* **323** 607–10
- [44] Hasegawa M, Mieszala M, Zhang Y C, Erni R, Michler J and Philippe L 2015 Orientation-controlled nanotwinned copper prepared by electrodeposition *Electrochim. Acta* **178** 458–67
- [45] Ye J C, Wang Y M, Barbee J T W and Hamza A V 2012 Orientation-dependent hardness and strain rate sensitivity in nanotwin copper *Appl. Phys. Lett.* **100** 261912
- [46] Lu L, Schwaiger R, Shan Z W, Dao M, Lu K and Suresh S 2005 Nano-sized twins induce high rate sensitivity of flow stress in pure copper *Acta Mater.* **53** 2169–79